In Situ Observations of the Deformation Behavior and Fracture Mechanisms of Ti-45Al-2Nb-2Mn + 0.8 vol pct TiB_2

ROCIO MUÑOZ-MORENO, CARL J. BOEHLERT, M. TERESA PÉREZ-PRADO, ELISA M. RUIZ-NAVAS, and JAVIER LLORCA

The deformation and fracture mechanisms of a nearly lamellar Ti-45Al-2Nb-2Mn (at. pct) + 0.8 vol pct TiB_2 intermetallic, processed into an actual low-pressure turbine blade, were examined by means of *in situ* tensile and tensile-creep experiments performed inside a scanning electron microscope (SEM). Low elongation-to-failure and brittle fracture were observed at room temperature, while the larger elongations-to-failure at high temperature facilitated the observation of the onset and propagation of damage. It was found that the dominant damage mechanisms at high temperature depended on the applied stress level. Interlamellar cracking was observed only above 390 MPa, which suggests that there is a threshold below which this mechanism is inhibited. Failure during creep tests at 250 MPa was controlled by intercolony cracking. The *in situ* observations demonstrated that the colony boundaries are damage nucleation and propagation sites during tensile creep, and they seem to be the weakest link in the microstructure for the tertiary creep stage. Therefore, it is proposed that interlamellar areas are critical zones for fracture at higher stresses, whereas lower stress, high-temperature creep conditions lead to intercolony cracking and fracture.

DOI: 10.1007/s11661-011-1022-3

I. INTRODUCTION

FOR the past three decades, two-phase α_2 (hexagonal close packed, DO_{19}) and γ (tetragonal, $L1_0$) titanium-aluminide (TiAl) intermetallics have been studied extensively as a potential group of materials for high-temperature structural applications. They present exceptional creep and oxidation resistance along with low density compared with nickel-based and cobalt-based superalloys.[1,2] In particular, TiAl-based intermetallics are targeted for high-temperature aerospace applications in low-pressure turbines (LPTs) because they can provide increased thrust-to-weight ratios and improved efficiency. LPT materials operate in aggressive environments at temperatures up to 1023 K (750 °C), and TiAl intermetallics are projected to replace the heavier nickel-based superalloys being used currently for such applications.[3]

TiAl matrix alloys reinforced with TiB_2 particles are well known to exhibit a lamellar microstructure with refined colony sizes caused by boron addition, which also provides strengthening. This is believed to assist the mechanical behavior, and in particular the fatigue and fatigue crack growth behavior. Mercer *et al.*[4] studied the fatigue crack growth behavior of three nearly lamellar (NL) alloys: Ti-47Al-2Cr-2Nb (at. pct), Ti-47Al-2Nb-2Mn (at. pct) + 0.8 vol pct TiB_2 and Ti-45Al-2Nb-2Mn (at. pct)* + 0.8 vol pct TiB_2. The fatigue crack growth rates for the TiB_2 containing alloys were slower than that for Ti-48Al-2Cr-2Mn, and Ti-45Al-2Nb-2Mn + 0.8 vol pct TiB_2 exhibited superior behavior. In addition, Recina[5] found that the fatigue lives of Ti–45Al–2Nb-2Mn + 0.8 vol pct TiB_2 at 873 K (600 °C) were longer than those for other NL alloys such as Ti-48Al-2W-0.5Si and Ti-48-2Cr-2Nb. Thus, the Ti-45Al-2Nb-2Mn + 0.8 vol pct TiB_2 intermetallic shows promise for LPT blades compared with other NL TiAl intermetallics.

In terms of the elevated-temperature creep resistance, it is well known that fully lamellar (FL) TiAl microstructures outperform equiaxed and duplex microstructures.[6–17] Systematically increasing the volume fraction of the lamellar constituent in a microstructure composed of equiaxed γ grains and colonies of $\gamma + \alpha_2$ lamellar leads to lower creep rates and extended creep lives.[8] In

*Henceforth, all alloy compositions are given in atomic percent.

ROCIO MUÑOZ-MORENO, Research Assistant is with the IMDEA Materials Institute, 28040 Madrid, Spain, and is also PhD Student, with the Department of Materials Science and Engineering, Universidad Carlos III de Madrid, 28911 Leganés, Spain. Contact e-mail: rocio.munoz@imdea.org CARL J. BOEHLERT, Associate Professor with the Department of Chemical Engineering and Materials Science, Michigan State University, East Lansing, MI 48824, is also a Visiting Professor with the IMDEA Materials Institute, and is also with the Department of Material Science, Polytechnic University of Madrid, 28040 Madrid, Spain. M. TERESA PÉREZ-PRADO, Senior Scientist, is with the IMDEA Materials Institute. ELISA M. RUIZ-NAVAS, Professor, is with the Department of Materials Science and Engineering, Universidad Carlos III de Madrid. JAVIER LLORCA, Director, is with the IMDEA Materials Institute, and is also a Professor with the Department of Materials Science, Polytechnic University of Madrid.

Manuscript submitted July 20, 2011.
Article published online December 10, 2011

addition, significantly reduced creep rates have been observed with finer lamellar spacings in FL polycrystalline microstructures containing $140 < \lambda < 660$ nm for Ti-47Al,[7] $120 < \lambda < 450$ nm for Ti-48Al,[8] $55 < \lambda < 400$ nm for Ti-45-2Nb-2Mn + 0.8 vol pct TiB_2,[15] where the characteristic lamellar spacing (λ) represents the average spacing of both the α_2 and γ lamellae. However, there is a limit below which the lamellae become unstable during elevated-temperature creep.[13,14] In addition, the tensile strength[15–18] of FL TiAl microstructures has been shown to be strongly dependent on lamellar spacing, where the strength increases with the refinement of λ down to 120 nm. Thus, it is believed that the elevated-temperature mechanical behavior of Ti-45-2Nb-2Mn + 0.8 vol pct TiB_2 can be improved through the refinement of λ, thereby making it more attractive for LPT blade applications.

However, the deformation evolution during the elevated-temperature tension, creep, and fatigue of NL or FL TiAl intermetallics has not been documented systematically. There are gaps in our understanding of the deformation and fracture behavior. In particular, the crack nucleation and propagation micromechanisms are not well understood. A better understanding of these fracture micromechanisms would shed light on the relative importance of the colony boundaries, lamellar interfaces, and the lamellar spacing in polycrystalline microstructures. This could lead to optimizing important microstructural features such as the lamellar spacings and colony sizes. Lu *et al.*[19] used room-temperature (RT) manual loading conditions to deform a Ti-49Al FL polycrystalline intermetallic. In their work, they imaged the deformation *in situ*. They found that interfacial microcracks were prevalent at RT. Cheng *et al.*[20] also studied the RT *in situ* deformation behavior of Ti-46Al-2Cr-0.2Si-0.1Nd and explained the toughening process through shear ligament formation. However, the literature is lacking on *in situ* characterization of the deformation and fracture behavior of TiAl intermetallics at elevated temperatures and during conditions other than tension or bending. *In situ* characterization techniques involving electron microscopy have been developed over the past decade to the point where high-resolution scanning electron microscope (SEM) images can be obtained *in situ* during elevated-temperature deformation involving tension, fatigue, and creep.[21–24] This type of characterization of the deformation behavior and deformation evolution of TiAl intermetallics would be beneficial to address the issue of when interlamellar, translamellar, and colony boundary fracture are prevalent.

The target of this work was to investigate the deformation evolution during RT and elevated-temperature tensile and tensile-creep deformation of a Ti-45Al-2Nb-2Mn + 0.8 vol pct TiB_2 intermetallic to obtain information that could be useful for improving the microstructure and thereby the mechanical properties. The tensile and tensile-creep deformation behavior was investigated using *in situ* experiments performed in a SEM. In this work, actual components in the form of LPT blades were manufactured and specimens were extracted from these blades for the microstructural and deformation characterization. Thus, the results presented are from actual components and are applicable to industrial conditions.

II. EXPERIMENTAL

The material was provided by Industria de Turbopropulsores S.A. (Madrid, Spain) in the form of LPT blades. The blades were centrifugal cast at the Institute of Metals Research of the Chinese Academy of Science (Shenyang, China). The nominal composition of the blades was Ti-45Al-2Mn-2Nb + 0.8 vol pct TiB_2, whereas the measured composition (in at. pct), using fluorescence was as follows: 50.94 pct Ti, 44.57 pct Al, 1.87 pct Nb, 1.16 pct Mn, 0.78 pct Si, 0.23 pct Ca, 0.39 pct Na, 0.05 pct K, and 0.01 pct P. The blades were hot isostatically pressed at 1533 K (1260 °C) and 140 MPa for 4 hours. They were then heat treated at 1353 K (1080 °C) for 8 hours in a vacuum furnace followed by furnace cooling. Metallographic samples were diamond cut and mounted in an epoxy resin. They were then polished using silicon carbide paper and diamond paste to a final finish of 0.06 μm using colloidal silica. A microstructure analysis was performed using optical microscopy (OM), SEM, and transmission electron microscopy (TEM). OM analysis was performed using an Olympus BX-51 optical microscope (Olympus America, Inc., Melville, NY). SEM analysis was performed using a Zeiss (Carl Zeiss, Jena, Germany) EVO MA15 equipped with an energy dispersive spectroscopy (EDS) system (Oxford INCAx-act; Oxford Instruments, Oxfordshire, UK). TEM analysis was performed using a FEI Instruments (Hillsboro, OR) Tecnai T20 TEM at 200 kV. The TEM foils were prepared by polishing the samples to a thickness of approximately 200 μm, punching 3 mm diameter disks, then thinning using a Struers (Struers A/S, Ballerup, Denmark) twinjet Tenupol-5 electropolisher until perforation. The electropolishing solution, which consisted of 5 pct perchloric acid, 35 pct butanol, and 60 pct methanol, was held at a constant temperature of 243 K (–30 °C) and 40 V. The volume fraction of the phases was measured using ImageJ (National Institutes of Health, Bethesda, MD) software on several backscattered electron (BSE) SEM images. The average colony size, taken from more than 60 measurements, was determined using the ASTM grain size standard.[25,26] λ was determined using several bright-field TEM images in the "edge-on" condition and dark-field imaging. The α_2 lamellar thickness was examined by isolating the (0001) α_2 diffraction spot of the [1120] α_2 selected area diffraction pattern (SADP), which overlaps the $\langle 110 \rangle$ SADP of the γ phase according to the $(0001)_{\alpha_2} \| \{111\}_{\gamma}, \langle 11\bar{2}0 \rangle_{\alpha_2} \| \langle 1\bar{1}0 |_{\gamma}$ Blackburn orientation relationship.[27] By comparing the α_2 lamellar width with λ, which constitutes the average lamellar width of both phases, the γ lamellae width was obtained. X-ray diffraction (XRD) was performed using a Philips (Almelo, The Netherlands) Panalytical model X'pert

PRO MRD system, and both intensity *vs* 2θ and pole figures plots were obtained.

In situ tensile and tensile-creep experiments were conducted. One sample was tensile tested at RT and four samples were tensile tested at an elevated temperature. Three elevated-temperature tensile-creep experiments were conducted. The samples were electrodischarge machined from the LPT blades with the geometry illustrated in Figure 1. The specimens were polished through a final finish of 0.06 μm. The *in situ* tests were performed using a screw-driven tensile stage placed inside the SEM. The temperature was controlled using a constant-voltage power supply to a 6-mm diameter tungsten-based heater located just below the gage section of the sample. An open-bath, closed-loop chiller was used to circulate distilled water at 288 K (15 °C) through copper tubes to prevent the tensile stage from overheating. A fine-gage K-type thermocouple was placed against the gage section of each sample. After the sample's gage-section temperature reached the desired creep temperature (973 K [700 °C]), a minimum of 30 minutes was given to stabilize the temperature prior to applying the load. The load was measured using a 4448 N load cell and was applied at 5 N/s until reaching the desired creep stress for the tensile-creep experiments. Secondary electron (SE) SEM images were taken before loading and at periodic displacements throughout the creep experiments without interrupting the experiment. The tensile tests were performed at RT and 973 K (700 °C) at a displacement rate of 0.004 mm/s $\left(\dot{\varepsilon} \cong 10^{-3}\text{seconds}^{-1}\right)$. The tensile test was interrupted at certain loads to acquire SEM images. The strain values were estimated from the displacement measurements taking into account the gage length of the samples. The pressure in the SEM chamber never exceeded 4×10^{-6} torr, and therefore, oxidation did not detrimentally affect the SEM imaging. Additional details of this apparatus and testing technique can be found elsewhere.[21–24] The fracture surfaces of failed samples were examined using SEM.

III. RESULTS

A. *Microstructure*

The polycrystalline microstructure exhibited a small fraction of α_2 and γ equiaxed grains located at colony boundaries. Thus, the microstructure was considered to be NL rather than FL (Figures 2 and 3). The boride-rich phase, which was identified using SEM/EDS analysis, was located both inside the colonies and at the colony boundaries with both globular and needle shapes, as observed previously.[28] The average volume fraction of the γ phase was 0.60 and the average volume fraction of the α_2 phase was 0.36. The average volume fraction of the boride-rich phase was 0.04. The colony size ranged from 52 μm to 636 μm, and typically, large colonies were surrounded by smaller colonies. The average colony size, as measured using 63 different colonies,

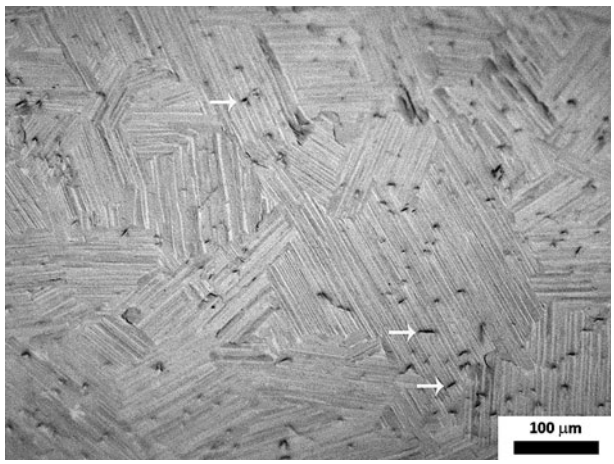

Fig. 2—OM photomicrograph showing the NL microstructure. The borides (see arrows) were dispersed both inside the colonies and at the colony boundaries.

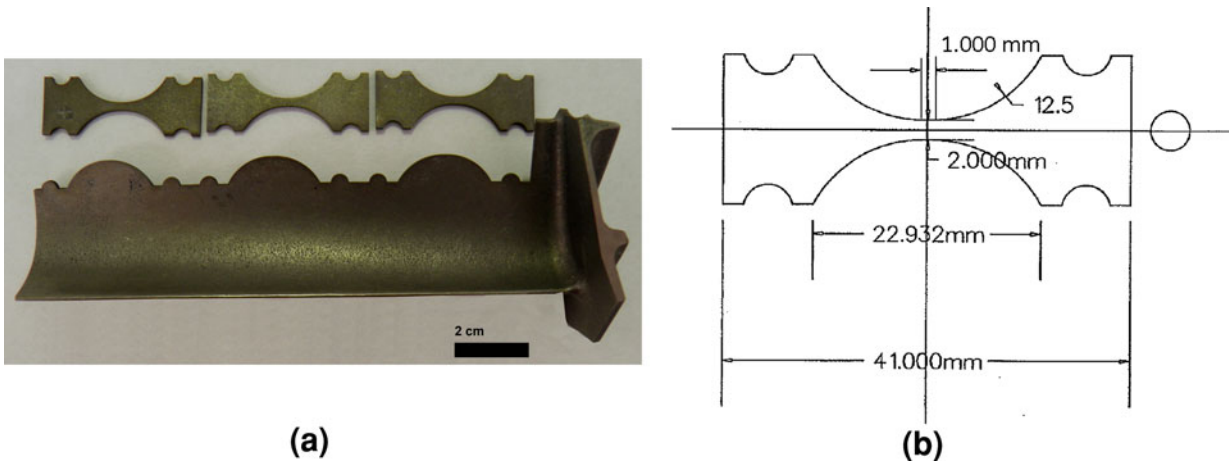

Fig. 1—The mechanical test specimens were electrodischarge machined from LPT blades as illustrated in (*a*). A schematic of the specimen geometry is provided in (*b*).

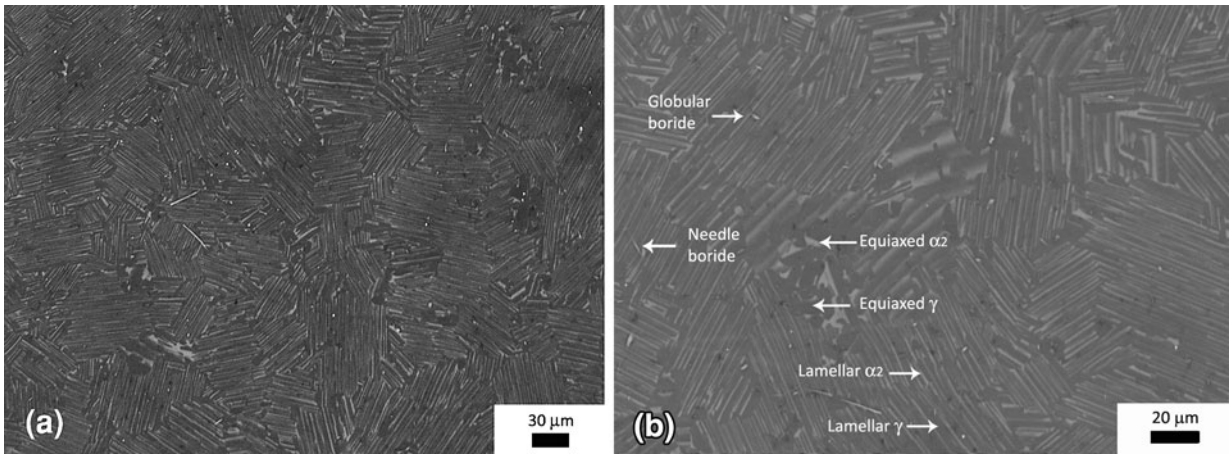

Fig. 3—(*a*) Low-magnification and (*b*) high-magnification BSE SEM photomicrographs of the NL microstructure, where the bright zones stand for the α_2 phase, the dark zones are the γ phase, and the areas with intermediate contrast represent the borides.

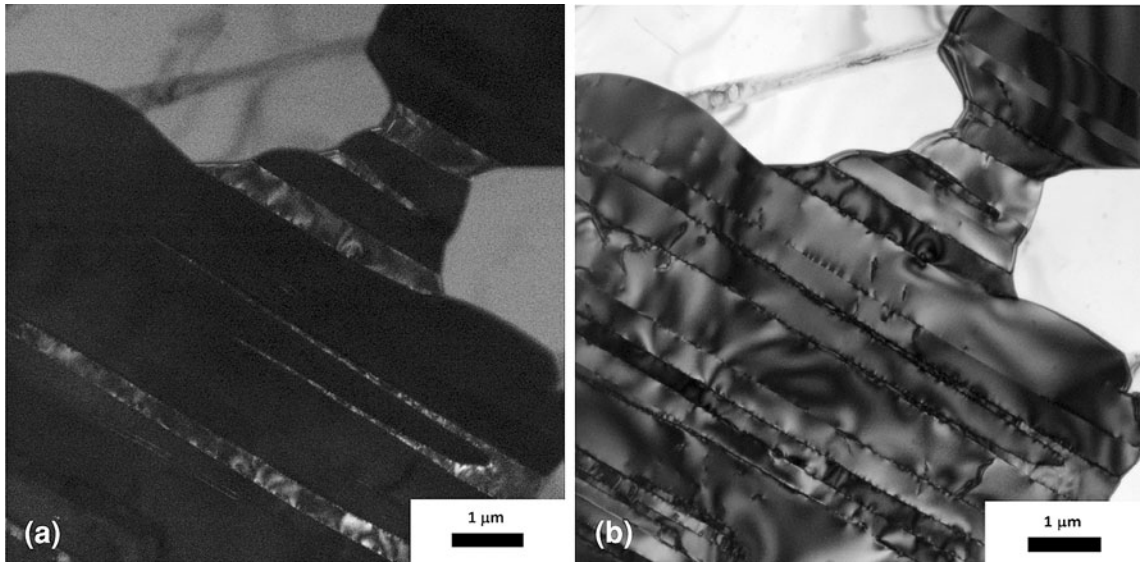

Fig. 4—(*a*) Dark-field (α_2 phase) and (*b*) bright-field TEM images taken from a lamellar region inside a colony.

was 195 μm and the standard deviation was 124 μm. Figure 4 illustrates representative TEM images. The average α_2 lamellar thickness was 287 $\pm$ 1 nm. The average γ phase lamellar thickness was 319 $\pm$ 1 nm, and λ was 297 $\pm$ 1 nm.

B. *Deformation and Fracture Behavior*

1. *Room-temperature tension*

The tensile tests indicated that the material was brittle at RT and the sample fractured at 480 MPa without any measurable plastic strain. No significant changes were characterized in the local microstructural patch observed during the *in situ* tests, and fracture occurred suddenly in a location outside that observed during the *in situ* imaging. This behavior is consistent with previous *in situ* observations of a similar FL TiAl intermetallic where the primary crack grew too rapidly to be observed.[20] Thus, the nucleation and growth of damage

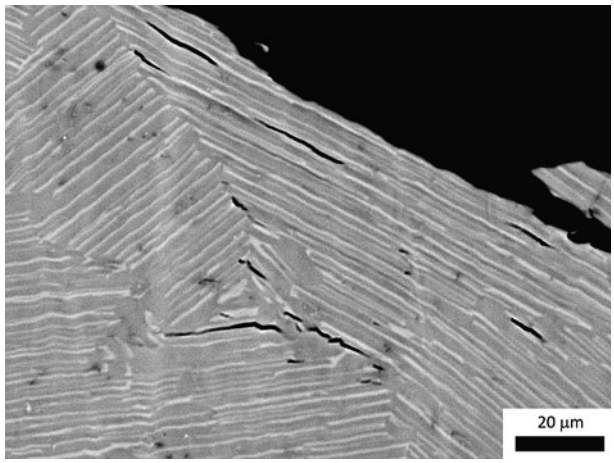

Fig. 5—BSE SEM photomicrograph of the RT tensile deformed microstructure illustrating interlamellar cracking below the fracture surface. The tensile axis was vertical.

during RT tensile deformation was not characterized in this study. The *postmortem* fracture observations showed interlamellar cracking (Figure 5) and cleavage fracture (Figure 6).

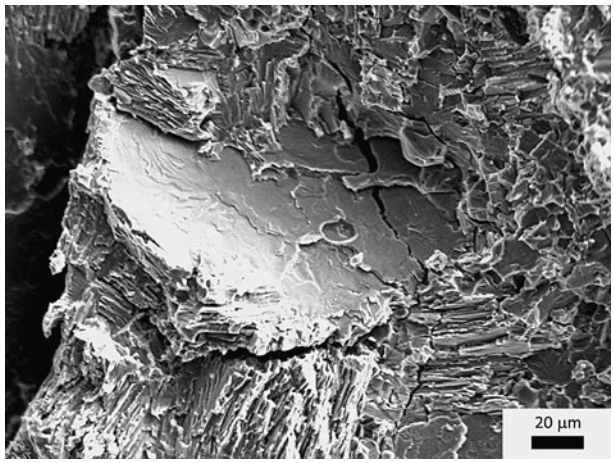

Fig. 6—SE SEM micrographs of the fracture surface of the sample tested at RT illustrating brittle features including cleavage.

2. *Elevated temperature*

a. Tension. During the elevated-temperature tensile tests, the sample exhibited a greater elongation-to-failure (ε_f) than at RT. The maximum tensile strength (σ_{max} = 520 MPa) was consistent with that reported in Reference 29 and was greater than the RT strength. This was a result of the higher ε_f and of the intermetallic's relative insensitivity to temperature up to T = 973 K (700 °C). Two different types of cracks were observed depending on their location. Only interlamellar cracks were found at the center of the gage section (Figures 7 and 8(a)). They developed at tensile stresses above 390 MPa and, thus, interlamellar cracking seems to activate in this material above a threshold stress (>0.75σ_{max}) at T = 973 K (700 °C). The boride-rich phase was also susceptible to cracking (Figure 9). In addition to interlamellar cracks, cracks perpendicular to the tensile axis grew from the sample edges (Figures 8(b) and (c)). They were assisted by the stress concentrations at the edges and propagated through the lamella and colonies. The fracture surfaces revealed ductile dimples and brittle cleavage (Figure 10).

b. Creep. Creep tests were carried out at 250 MPa, which represented 0.48σ_{max} at 973 K (700 °C). The creep behavior presented the three typical stages. However,

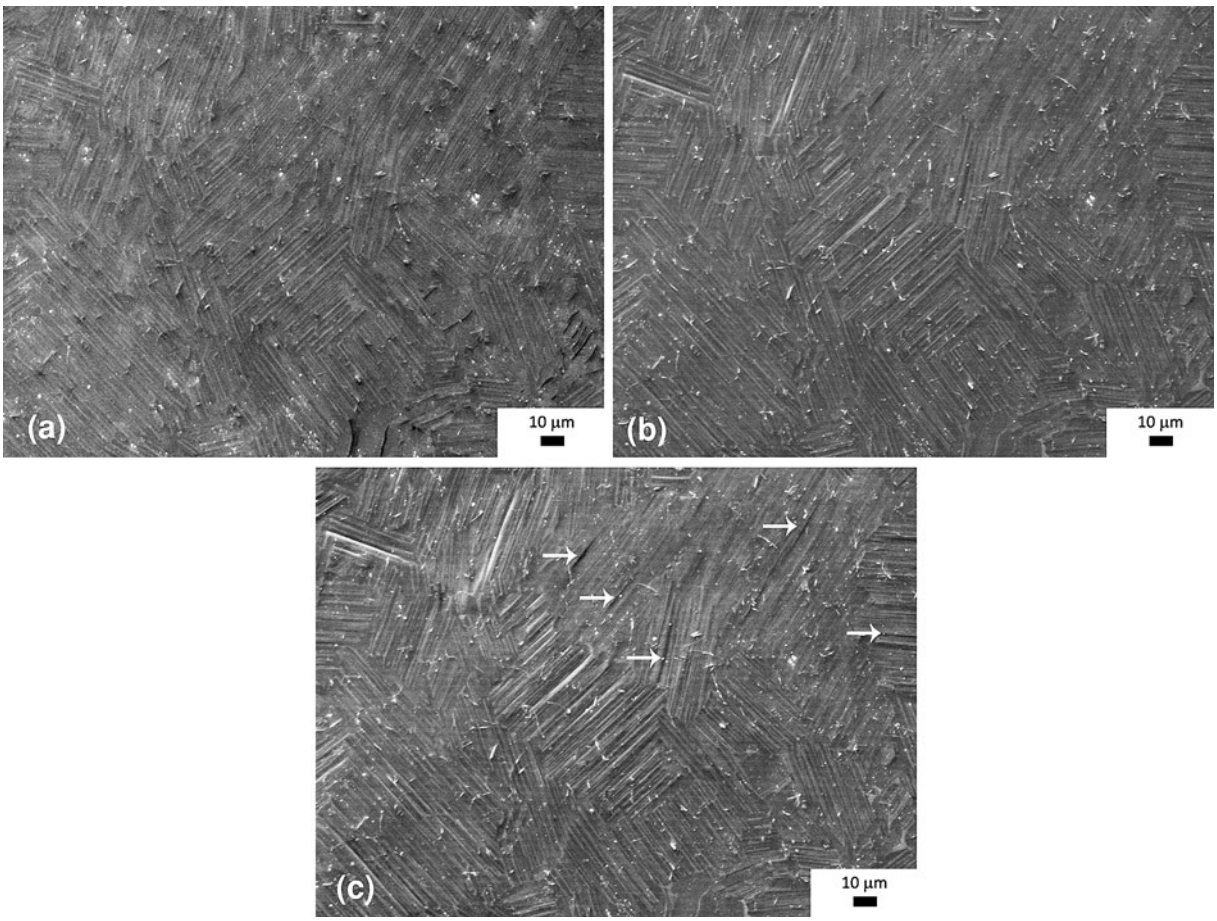

Fig. 7—SE SEM micrographs obtained during *in situ* tensile testing at 973 K (700 °C). The tensile stress was (*a*) 0 MPa, (*b*) 413MPa, and (*c*) 481MPa. The onset of interlamellar cracking is evident in (*c*). The tensile axis was vertical.

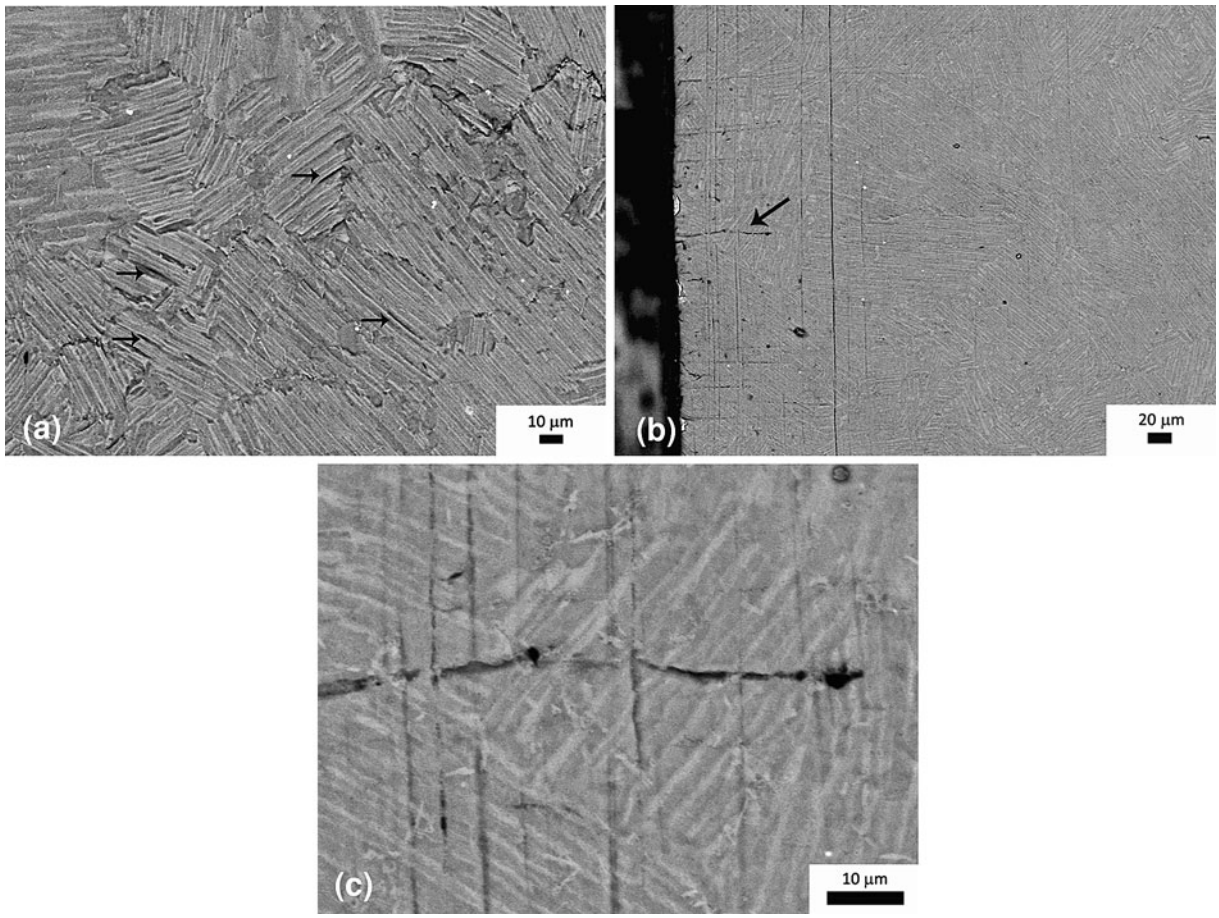

Fig. 8—BSE SEM micrographs obtained during *in situ* tensile testing at 973 K (700 °C) at an applied stress of 396 MPa. (*a*) Onset of interlamellar cracking in the center of the sample. (*b*) Cracks perpendicular to the vertical loading axis emanating from the edge. (*c*) Higher magnification image of the area indicated by the black arrow in (b) showing that the cracks propagated through the lamella and colonies. Note that the vertical lines in (b) and (c) were polishing artifacts present before loading.

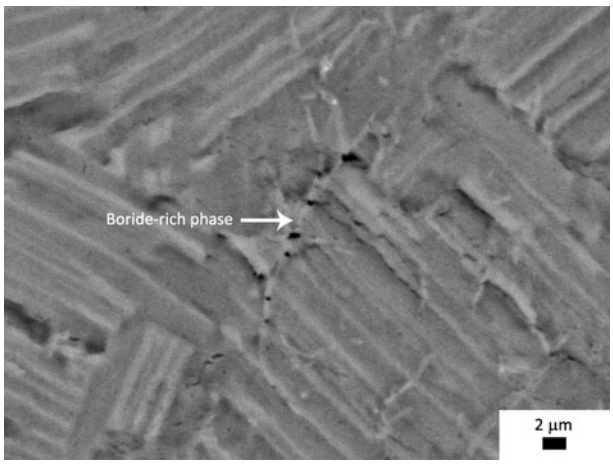

Fig. 9—BSE SEM micrograph showing multiple cracks within the boride-rich phase during a tensile test at 973 K (700 °C). The loading axis was vertical.

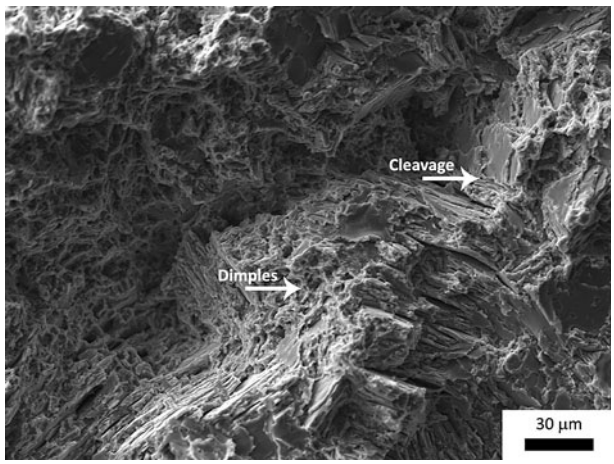

Fig. 10—SE SEM micrograph of the fracture surface after tensile testing at 973 K (700 °C). Both ductile (dimples) and brittle (cleavage) features were observed.

the length of the secondary creep regime was not well defined as the creep rates increased slightly shortly after achieving the minimum creep rate and continued to increase throughout the remainder of the experiment. Low-magnification SEM micrographs obtained during each of the three stages of creep are shown in Figure 11.

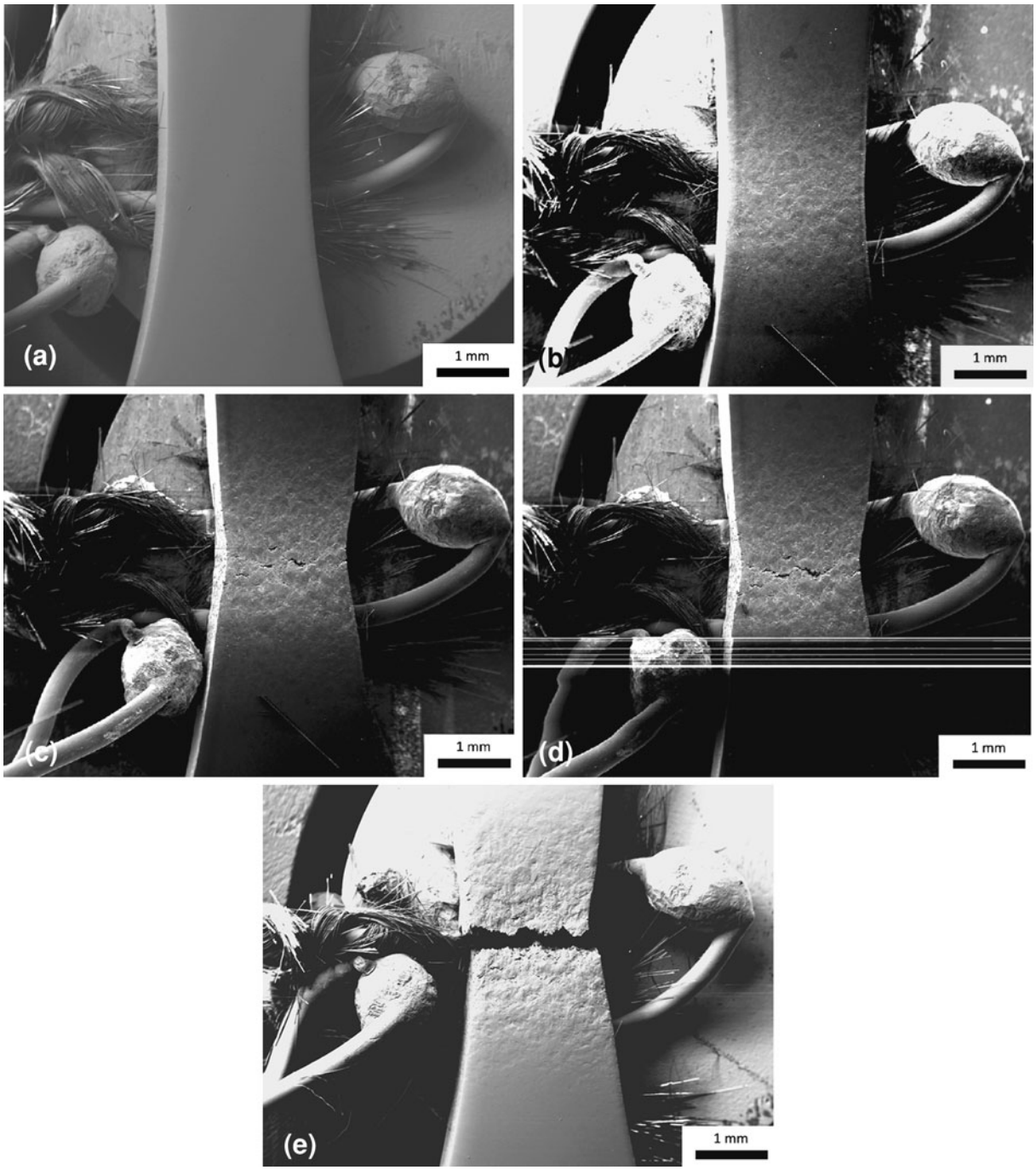

Fig. 11—Sequence of low-magnification SE SEM micrographs obtained during the creep experiment. (*a*) 0 hours; (*b*) secondary creep stage, 18.7 h, $\varepsilon \sim 1.6$ pct; (*c*) tertiary creep stage, 23.8 h, $\varepsilon \sim 3.0$ pct; (*d*) tertiary creep stage just prior to fracture, 25.9 h, $\varepsilon \sim 3.2$ pct; and (*e*) after fracture. The tensile axis was vertical.

Unlike the elevated-temperature tensile tests, colony boundaries were the primary sites for crack nucleation and propagation. During the secondary creep regime and continuing into the tertiary creep regime, surface relief was increasingly evident suggesting that the colony boundaries were deforming through boundary sliding leading to intercolony cracking. Cracking initiated at colony boundaries in the center of the gage section and propagated along the colony boundaries (Figure 12). Edge cracks were also observed during the experiment (Figure 13). Ductile dimples were dominant in the fracture surface, although some cleavage fracture was also found (Figure 14).

IV. DISCUSSION

A. *Microstructure*

Centrifugal casting of TiAl intermetallics has been shown to be a cost-effective processing technique for

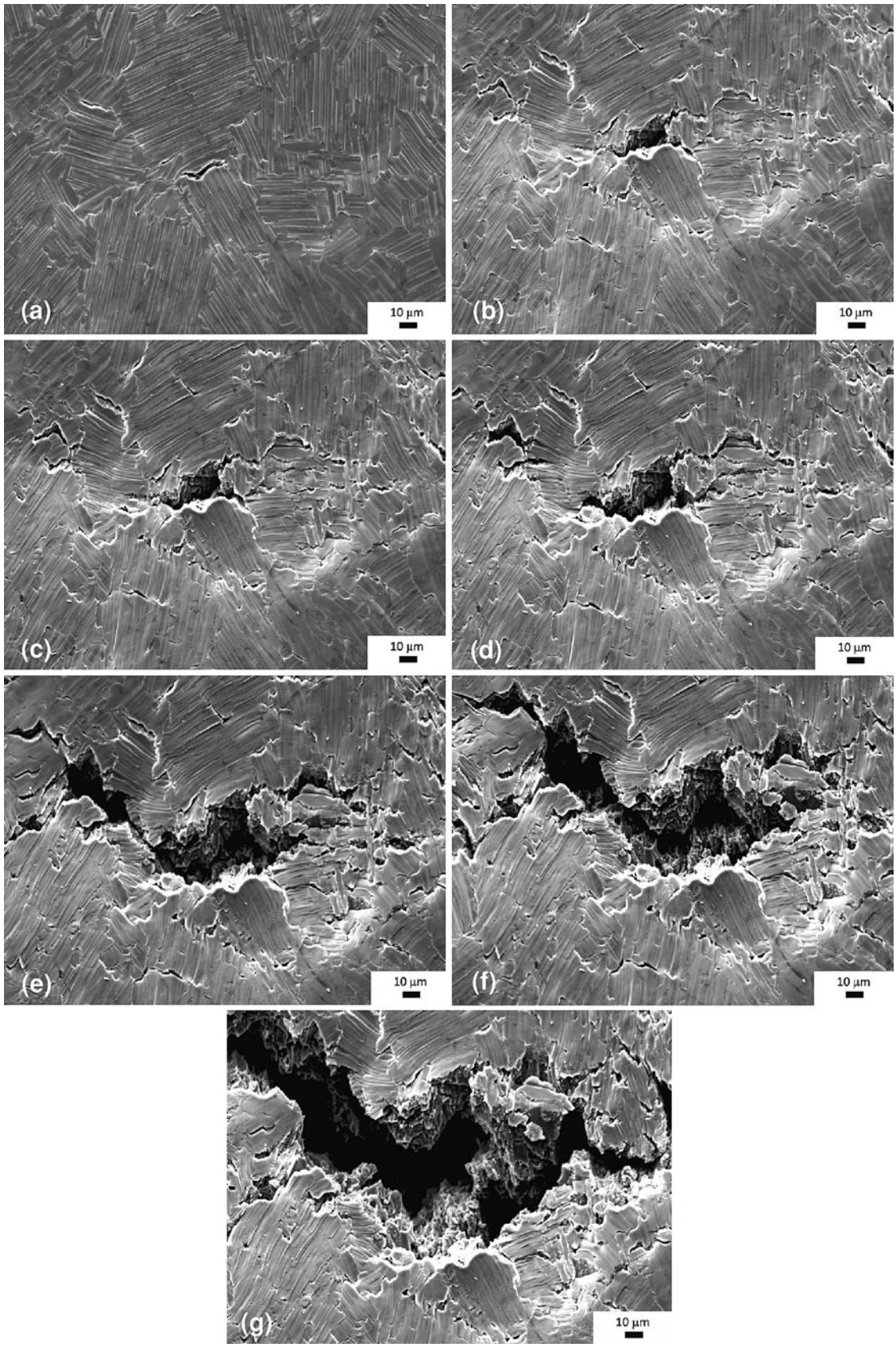

Fig. 12—SE SEM micrographs illustrating the nucleation and growth of the primary crack, which led to fracture in the creep test. (*a*) 7.6 h, $\varepsilon \sim 2.0$ pct; (*b*) 22.1 h, $\varepsilon \sim 2.1$ pct; (*c*) 22.4 h, $\varepsilon \sim 2.2$ pct; (*d*) 22.8 h, $\varepsilon \sim 2.5$ pct; (*e*) 23.1 h, $\varepsilon \sim 2.6$ pct; (*f*) 23.4 h, $\varepsilon \sim 2.7$ pct; and (*g*) 24.1 h, $\varepsilon \sim 3.2$ pct. Note that the crack initiated and grew along the colony boundaries. The tensile axis was vertical.

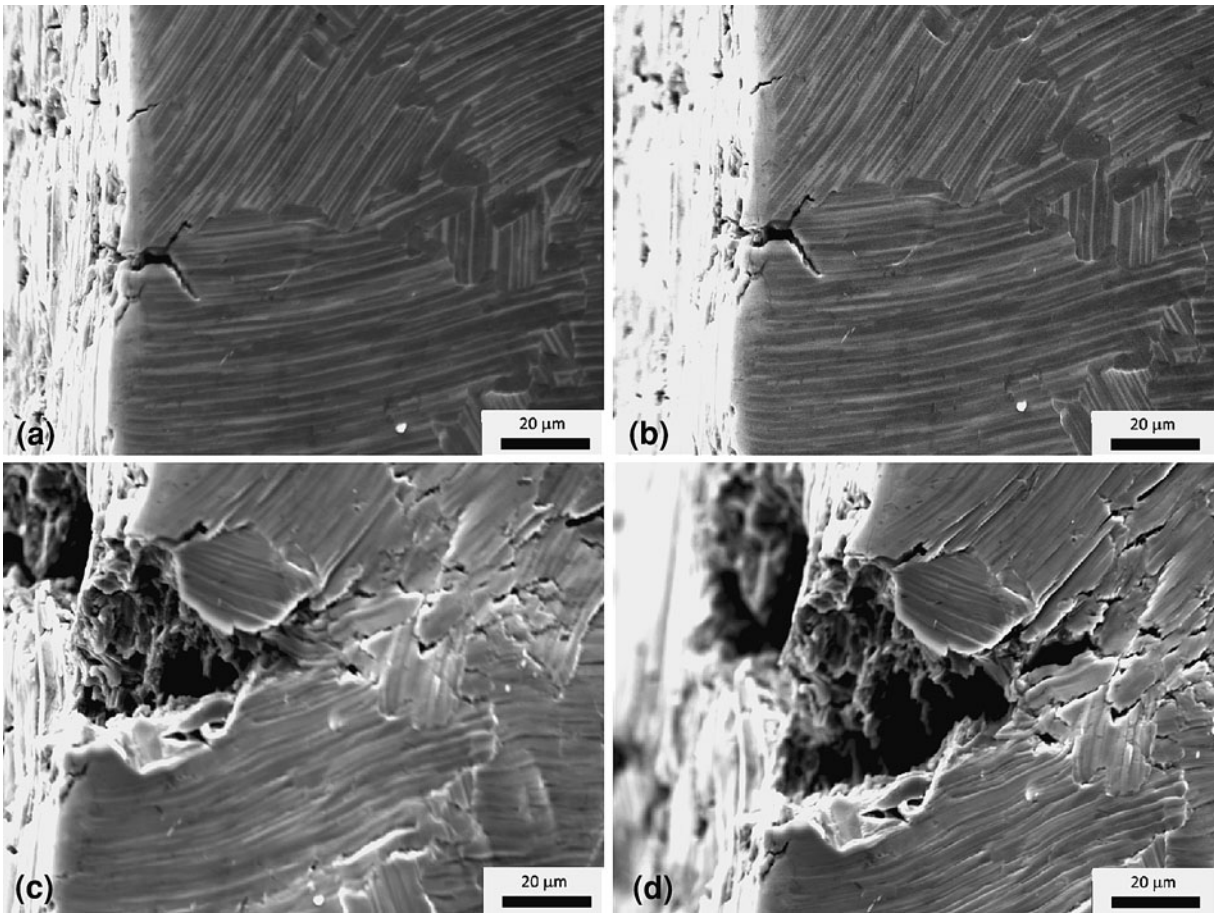

Fig. 13—SE SEM micrographs illustrating the nucleation and growth of a secondary edge crack during creep. (*a*) 5.9 h, $\varepsilon \sim 1.2$ pct; (*b*) 6.6 h, $\varepsilon \sim 1.8$ pct; (*c*) 22.3, $\varepsilon \sim 2.2$ pct; and (*d*) 22.7 h, $\varepsilon \sim 2.4$ pct. The tensile axis was vertical.

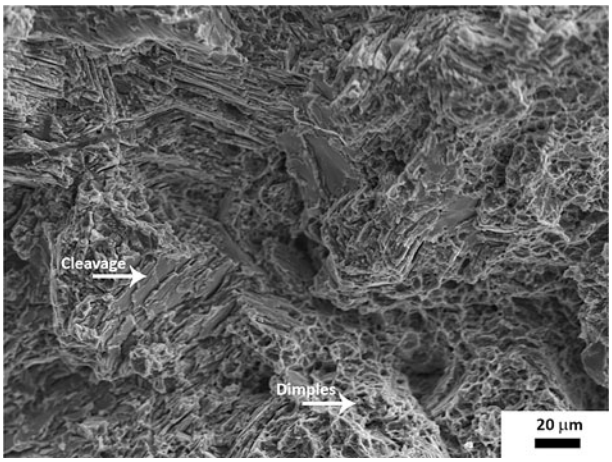

Fig. 14—SE SEM micrograph of a fracture surface after a creep test. The ductile dimples were dominant although brittle cleavage features were also present.

making automotive valves. In fact a Ti-45Al-8Nb intermetallic, produced using centrifugal casting, has passed engine tests.[30] From the microstructure analysis, it was evident that centrifugal casting of Ti-45Al-2Nb-2Mn + 0.8 vol pct TiB_2 results in a NL polycrystalline microstructure. In addition, other techniques, such as investment casting, powder metallurgy, and spark plasma sintering, have been used to produce NL microstructures. In centrifugal cast automotive valves and powder metallurgy processed intermetallics, the average colony size was finer than 50 μm.[30,31] Seo *et al.*[32] obtained an average colony size lower than 100 μm for investment casting. For spark-plasma sintering Ti-47Al-2Cr-2Nb, the average colony size was approximately 150 μm,[33] whereas the average colony size for an investment cast Ti-45Al-2Nb-2Mn + 0.8 vol pct TiB_2 intermetallic ranged between 20 and 100 μm.[15] In the current material, the size distribution of the colonies was large (52 to 634 μm), a feature that may be associated with the abnormal geometry of the centrifugal cast blade. It was noted that large colonies were surrounded by smaller colonies. Thus, large colonies grew at the expense of smaller ones. This may have influenced the mechanical behavior, and in particular the creep behavior, where cracking was observed primarily at colony boundaries. The average lamellar spacing of the studied intermetallic (γ width = 319 nm;

α_2 width = 287 nm) was similar to that of an investment cast Ti-45Al-2Nb-2Mn + 0.8 vol pct TiB_2 intermetallic (γ width = 480 nm; α_2 width = 173 nm).[32]

B. *Deformation and Fracture Mechanisms*

1. *Tension*

If each colony is assumed to behave as a monocrystal, such as polysynthetically twinned materials, the deformation behavior would be dependent on the orientation of the lamellae with respect to the loading axis.[34–36] Brittle behavior is typical, along with high strength and low ε_f, for lamellar orientations of 0 deg or 90 deg with respect to the load axis. Such conditions result in extremely low ε_f values as a result of atomic plane separation (perpendicular case) or translamellar fracture (parallel case). If the lamellae are oriented at 45 deg with respect to the loading direction, the strength is lower and the material presents a higher ε_f. For this so-called soft mode, the deformation will take place because of dislocation slip resulting from the presence of a shear component of the applied stress along the interlamellar boundaries, and the dominant fracture mode is interlamellar. Polycrystalline microstructures, containing randomly oriented lamellae, are expected to exhibit a mixed fracture mode composed of interlamellar and translamellar cracking together with decohesion at the colony boundaries.[37,38]

Lu *et al.*[19] used RT manual loading conditions to obtain *in situ* observations of a Ti-49Al FL polycrystalline microstructure. Their results indicated that when the lamellae within a colony were oriented at a large angle from the tensile axis, the main crack propagated through linking with interlamellar microcracks by shearing or tearing. When the lamella within a colony were nearly parallel to the loading direction, the main crack propagated in a translamellar fashion linking with the two types of microcracks, which were interlamellar and translamellar. When the main cracks propagated along the colony boundaries, the microcracks usually formed in interlamellar or translamellar directions in neighboring grains, depending on the orientation of the lamellae with respect to the main crack. When the main crack encountered a nearly transverse colony boundary, intercolony fracture occurred. Their results are similar to those observed in this study as interlamellar and translamellar cracking were found during the *in situ* tensile experiments.

During the elevated-temperature experiments, the onset and propagation of damage could be followed more closely through *in situ* observations because of the larger ε_f. Combining the observations from the RT and elevated-temperature tensile experiments, interlamellar cracking seemed to be the dominant cracking mode. The interlamellar cracking was observed only at stresses greater than 390 MPa independent of the test temperature. This observation is important as it suggests that the interface strength between the lamellae is greater than 390 MPa. It is expected that this value will be dependent on the microstructure, and the current value may be unique for the microstructure of this manufactured LPT blade.

2. *Creep*

During the tensile-creep experiments, no or limited interlamellar cracking was observed. The creep applied stress, σ = 250 MPa, was significantly lower than 390 MPa. The higher-stress elevated-temperature tensile test presented more interlamellar cracking, whereas the lower-stress creep test presented intercolony cracking. Thus, interlamellar cracking seems to be the dominant cracking mechanism when the stresses are high ($>0.75\sigma_{max}$), whereas interlamellar cracking is inhibited during diffusion-assisted deformation at elevated temperatures under relative low stresses ($<0.50\sigma_{max}$). Under these latter conditions, intercolony cracking controls the onset of damage as the diffusion rates across the colony boundaries are expected to assist the deformation at such locations. This can lead to local deformation at colony boundaries and thus explain the enhanced colony boundary deformation in the form of relief and sliding. It has been proposed that sliding occurs by the glide and climb of extrinsic lattice dislocations in grain boundary zones and is related to the buildup of dislocations near grain boundaries.[39] The stress concentration caused by grain-boundary dislocation pileup can be relieved by activating grain-boundary dislocation sources or by nucleating and propagating an intergranular crack. Thus, cracking can serve as an accommodation mechanism for grain boundary sliding. The *in situ* observations were useful in confirming both the crack propagation along the colony boundaries as well as the minimum stress level necessary to initiate interlamellar cracking.

Colony boundary cracking has been reported in previous *ex situ* experiments of this alloy.[13,15] For example, Zhu *et al.*[13] studied the creep behavior of a NL Ti-45Al-2Nb-2Mn + 0.8 vol pct TiB_2 in microstructures with different lamellar spacing at 1033 K (760 °C) for applied stresses between 138 and 207 MPa. The minimum creep rate $\dot{\varepsilon}$ from their work for a NL alloy with λ = 400 nm was 7.7×10^{-8} seconds^{-1} at σ = 207 MPa.[13] This value was close to that measured in the current study $\left(\dot{\varepsilon} = 1 \times 10^{-7}\,\text{seconds}^{-1}\right)$ where λ = 297 nm, σ = 250 MPa, and T = 973 K (700 °C). In addition, Zhu *et al.*[13] affirmed that the NL microstructures containing larger λ values exhibited higher creep strain rates than those with lower λ. Microstructures containing refined λ (<20 nm) may not be desirable for creep-driven applications as they are not stable during the creep deformation, as has been observed in a Ti-46Al intermetallic.[14] The *in situ* observations of the current work suggested that the microstructure (λ = 297 nm) was stable at least for up to 72 hours of creep at σ = 250 MPa.

V. SUMMARY AND CONCLUSIONS

The deformation and fracture behavior of a nearly-lamellar Ti-45Al-2Nb-2Nb + 0.8 pct TiB_2 intermetallic, processed into LPT blades, was analyzed by means of *in situ* tensile and tensile-creep experiments performed inside a SEM. Interlamellar and translamellar cracking was observed during the RT tensile experiments in

combination with a brittle fracture. The elevated-temperature tensile experiments highlighted the deformation and fracture evolution, and showed that the minimum stress necessary for interlamellar cracking was approximately 390 MPa for this material. Below this threshold, intercolony cracking was the dominant failure micromechanism, as shown in the creep experiments carried out at 250 MPa. Therefore, it is proposed that interlamellar areas are critical zones at higher stresses, whereas lower-stress, high-temperature creep conditions promote intercolonial cracking and fracture.

ACKNOWLEDGMENTS

The authors are grateful to Industria de Turbo Propulsores, S.A. for supplying the intermetallic blades. Funding from the Spanish Ministry of Science and Innovation through projects MAT2009-14547-C02-01 and MAT2009-14547-C02-02 is acknowledged. The Madrid Regional Government supported this project partially through the ESTRUMAT grant P2009/MAT-1585. C.J.B. acknowledges the support from Grant SAB2009-0045 from the Spanish Ministry of Education for his sabbatical stage in Madrid.

REFERENCES

1. E.A. Loria: *Intermetallics*, 2000, vol. 8, pp. 1339–45.
2. M. Yamaguchi, H. Inui, and K. Ito: *Acta Mater.*, 2000, vol. 48, pp. 307–22.
3. G. Lütjering and J.C. Williams: *Titanium. Engineering Materials and Processes.*, 2nd ed., Springer-Verlag, Berlin, 2007, pp. 337–66.
4. C. Mercer, J. Lou, S.M. Allameh, and W.O. Soboyejo: *Metall. Mater. Trans. A*, 2001, vol. 32A, pp. 2781–94.
5. V. Recina: *Mater. Sci. Technol.*, 2000, vol. 16, pp. 333–40.
6. T.A. Parthasarathy, M.G. Mendiratta, and D.M. Dimiduk: *Scripta Mater.*, 1997, vol. 37 (3), pp. 315–21.
7. T.A. Parthasarathy, M. Keller, and M.G. Mendiratta: *Scripta Metall.*, 1998, vol. 38 (7), pp. 1025–31.
8. J. Beddoes, L. Zhao, P. Au, D. Dudzinski, and J. Triantafillou: *Structural Intermetallics*, TMS, Warrendale, PA, 1997, pp. 109–18.
9. W.R. Chen, J. Triantafillou, J. Beddoes, and L. Zhao: *Intermetallics*, 1999, vol. 7, pp. 171–78.
10. K. Maruyama, R. Yamamoto, H. Nakakuki, and N. Fujitsuna: *Mater. Sci. Eng. A*, 1997, vols. 239, 240, pp. 419–28.
11. C.E. Wen, K. Yasue, J.G. Lin, Y.G. Zhang, and C.Q. Chen: *Intermetallics*, 2000, vol. 8, pp. 525–29.
12. H.S. Park, S.K. Hwang, C.M. Lee, Y.C. Yoo, S.N. Nam, and N.J. Kim: *Metall. Mater. Trans. A*, 2001, vol. 32A, pp. 251–59.
13. H. Zhu, D.Y. Seo, K. Mayurama, and P. Au: *Mater. Sci. Eng. A*, 2008, vols. 483–484, pp. 533–36.
14. C.J. Boehlert, D.M. Dimiduk, and K.J. Hemker: *Scripta Mater.*, 2002, vol. 46 (4), pp. 259–67.
15. H. Zhu, D.Y. Seo, and P. Au: *Scripta Mater.*, 2006, vol. 54, pp. 1979–84.
16. P.M. Hazzledine and D.M. Dimiduk: *Structural Intermetallics*, TMS, Warrendale, PA, 1997, pp. 481–87.
17. J.N. Wang and K. Xie: *Intermetallics*, 2000, vol. 8, pp. 545–48.
18. G. Cao, L. Fu, J. Lin, Y. Zhang, and C. Chen: *Intermetallics*, 2000, vol. 8, pp. 647–53.
19. Y.H. Lu, Y.G. Zhang, L.J. Qiao, Y.B. Wang, C.Q. Chen, and W.Y. Chu: *Intermetallics*, 2000, vol. 8, pp. 1443–45.
20. J. Cheng, W. Jianguo, and C. Wenjue: *Scripta Metall. Mater.*, 1995, vol. 32 (10), pp. 1579–84.
21. C.J. Boehlert, S.C. Longanbach, and T.R. Bieler: *Phil. Mag.*, 2008, vol. 88 (5), pp. 641–64.
22. C.J. Boehlert, C.J. Cowen, S. Tamirisakandala, D.J. McEldowney, and D.B. Miracle: *Scripta Mater.*, 2006, vol. 55, pp. 465–68.
23. C.J. Cowen and C.J. Boehlert: *Metall. Mater. Trans. A*, 2007, vol. 38A, pp. 26–34.
24. W. Chen and C.J. Boehlert: *Int. J. Fatigue*, 2010, vol. 32 (5), pp. 799–807.
25. J.E. Hilliard: *Metall. Progr*, 1964, vol. 78, pp. 99–100.
26. ASTM E112-96e3, Standard Test Methods for Determining Average Grain Size.
27. M.J. Blackburn: *The Science, Technology and Application of Titanium*, R.I. Jaffe and N.E. Promisel, eds., Pergamon Press, Oxford, UK, 1970, p. 663.
28. D.E. Larsen, S. Kampe, and L. Christodoulou: *Mater. Res. Soc. Symp. Proc.*, 1990, vol. 194, p. 285.
29. R.A. Mirshams, Z.X. Li, and H.P. Mohamadian: *J. Mater. Sci. Lett.*, 1997, vol. 16, pp. 715–18.
30. K. Liu, Y.C. Ma, M. Gao, G.B. Rao, Y.Y. Li, K. Wei, X. Wu, and M.H. Loretto: *Intermetallics*, 2005, vol. 13, pp. 925–28.
31. Y.H. Wang, J.P. Lin, Y.H. He, Y.L. Wang, and G.L. Chen: *J. Alloys Compd.*, 2009, vol. 468, pp. 505–11.
32. D.Y. Seo, L. Zhao, and J. Beddoes: *Mater. Sci. Eng. A*, 2002, vols. A329–331, pp. 130–40.
33. A. Couret, G. Molénat, J. Galy, and M. Thomas: *Intermetallics*, 2008, vol. 16, pp. 1134–41.
34. T.A. Parthasarathy, P.R. Subramanian, M.G. Mendiratta, and D.M. Dimiduk: *Acta Mater.*, 2000, vol. 48, pp. 541–51.
35. M. Hazzledine and B.K. Kad: *Mater. Sci. Eng. A*, 1995, vol. 192 (193), pp. 340–46.
36. H. Inui, M.H. Oh, A. Nakamura, and M. Yamaguchi: *Acta Metall. Mater.*, 1992, vol. 40 (11), pp. 3095–104.
37. F. Appel and M. Oehring: *GKSS Research Center Geesthacht GmbH, Geesthacht, Germany, Titanium and Titanium Alloys: Fundamentals and Applications*, Wiley-VCH, Weinheim, Germany, 2003, pp. 89–152.
38. F. Appel: *Intermetallics*, 2001, vol. 9, pp. 907–14.
39. T.G. Langdon: *Phil. Mag.*, 1970, vol. 22, pp. 689–700.